Improved accuracy for calibrated mass distribution measurements of bimetallic nanoparticles

Kaleb J. Duelge [a,b,1], George W. Mulholland [a,b,1], Antonio R. Montoro Bustos [a,1], Michael R. Zachariah [a,b,c], John M. Pettibone [a,1,*]

[a] National Institute of Standards and Technology, Gaithersburg, MD, USA
[b] University of Maryland, College Park, USA
[c] University of California, Riverside, USA

ABSTRACT

Implementation of hybrid nanoparticles (HNPs), consisting of two different metal components, into applied systems has been hindered by an incomplete understanding of structural and chemical properties responsible for their enhanced, yet inconsistent performance. To address this persistent need, our work focused on using the electrospray differential mobility analyzer hyphenated to inductively coupled plasma mass spectrometry (ES-DMA-ICP-MS) to determine mass distributions across the entire NP distribution. Although previous work had applied similar hyphenated measurements to HNP systems, no efforts to develop accurate calibration methods for quantifying NP, and especially HNP, masses have been reported. We chose gold titania catalyst HNPs (Au@TiO$_2$: 4 nm gold NPs adsorbed on 100 nm–300 nm TiO$_2$ NPs) as a representative system because a large body of research exists on this topic. When we used ionic standards and compared it to our Au@TiO$_2$ control, a reproducible difference in the slope was observed that led to an overestimation of both gold (Au) and titanium (Ti) by nearly a factor of four for the HNPs, demonstrating the complexity of quantification and the need to both develop a validated calibration method and identify the major sources for uncertainty in quantification. We determined the mass quantification discrepancy derived from the metal oxide NPs (independent of the presence of Au) and was caused by the DMA and ES (not the ICP-MS). Corrections were made for multiple charging that significantly improved the agreement between the ionic standard and Au@TiO$_2$ metal quantification. Discussion on material properties for improved accuracy across different shapes, sizes, compositions, and surface chemistries is also included to demonstrate the general utility of the calibration across a broad number of fields. ES-DMA-ICP-MS is a powerful technique that provides statistically significant data for simultaneous determination of mass distributions of multi-element HNP systems across the entire sample population and should enhance characterization and development of HNPs when coupled with current core methods.

1. Introduction

Supported metallic NPs are of broad interest due to their tunable optical (Lee et al., 2013), antimicrobial (Ashfaq et al., 2016), and

---

catalytic properties (Enache et al., 2006; Sankar et al., 2012; Turner et al., 2008). Because of their promise in various applications, many demonstrations for their use have been reported, where modifying NP size, interfacial properties, composition ratios, and surface structure has led to tuning variables for controlled optical and electronic properties (White et al., 2009). Specifically for spatial and geometrical control over supported NPs through ligand chemistry, higher sensitivity surface-enhanced Raman scattering, improved and selective antimicrobial behavior, and enhanced catalytic performance have been demonstrated. The catalytic performance has been an accelerant in the research and development for elucidating structure-function properties for improved design rules (Holm et al., 2020). Because the enhanced reactivity is due to active sites on the supported metal structure within the hybrid material, approaches such as deposition and direct growth onto larger supports are used to preserve the size, and thus catalytic properties, of the active supported structures. However, variation in batch-to-batch performance is significant and reproducibility of NP synthesis, assembly, and activation of their properties have been persistent challenges for more than two decades (Liao et al., 2015).

Identifying specific material structure-property relationships for better design, higher performance, and limiting batch-to-batch variability for commercial and industrial applications will require improved methods for characterizing a more complete NP population, instead of trying to find the "needle-in-haystack" subpopulation that may be responsible for most of the observed enhanced property of interest. Physical characterization has proven difficult and primarily consists of microtomic and microscopic analyses, such as high-angle annular dark-field scanning-transmission electron microscopy and tomography (Chan & Barteau, 2005; Prieto et al., 2013; Weyland et al., 2001), and bright-field transmission electron microscopy (TEM) (Munnik et al., 2014; Yang et al., 2017). The spatial atomic distribution is often measured by energy dispersive X-ray spectroscopy and further chemical characterization has also included additional spectroscopy methods (e.g., using electron energy loss spectroscopy). All these techniques are limited by the small sample size, which often consists of single NPs per image, and statistically significant sampling of the populations can be intractable (Sharma et al., 2019). Alternative approaches that can acquire similar information, provide a more statistical representation of the property of interest, and be higher throughput are necessary for both research and manufacturing applications. One ensemble measurement is small-angle X-ray scattering, which was previously used to differentiate homogeneous and heterogenous spatial loading of small copper catalyst NPs in mesoporous silica supports (Gommes et al., 2015). Another option is the differential mobility analyzer combined with inductively coupled plasma mass spectrometry (DMA-ICP-MS). This developing technique consists of DMA, an aerosol electrical mobility measurement that classifies NPs by size, and ICP-MS, an elemental analysis technique to determine mass quantities. The combined technique can give the mass concentration of multiple elements across the NP size distribution. Some examples include measurements of laser ablation products (Saetveit et al., 2008), protein NPs (Carazzone et al., 2008), lead nitrate NPs (Myojo et al., 2002), and platinum loading and release from gold nanoparticles (AuNPs) (Tan et al., 2018). The ICP-MS can also be run in single particle mode (sp-ICP-MS) in which individual NPs are quantified in dilute samples via a rapid analysis mode (dwell time on the order of μs – ms) (Bustos & Winchester, 2016). DMA-ICP-MS run in single particle mode (DMA-sp-ICP-MS) has been used to distinguish aggregates from primary NPs (Tan et al., 2016) and to determine the geometry of nanorods (Tan et al., 2019).

While DMA-ICP-MS has been used for various applications, the calibration of measurements has been limited. A simple calibration method for DMA-ICP-MS is lacking, specifically for elements that do not have a relevant NP reference material. DMA-sp-ICP-MS measurements have been calibrated by standard methods used for sp-ICP-MS measurements: a NP of known mean diameter is measured and the sphere equivalent mass is assigned to the mean ICP-MS response (Pace et al., 2011; Tan et al., 2016). Validation of the rotating disk diluter scanning mobility particle sizer ICP-MS consisted of comparisons between mass distributions derived from number distributions from the condensation particle counter (CPC) detector, and mass distributions from the ICP-MS (Hess et al., 2016). Another approach calibrated the total mass from the DMA-ICP-MS distribution by relating the DMA-ICP-MS response to the total number measured by the DMA-CPC for a standard of well-known total mass, density, and average NP size (Elzey et al., 2013). Alternatively, it was suggested to use the known total mass of AuNP reference materials (Elzey et al., 2013). A direct comparison to an ionic standard should in principle be sufficient to calibrate the measurement. We used this approach to test the calibration of synthesized Au@TiO$_2$ HNPs following a procedure reported to prepare catalysts (Holm et al., 2020). Here we developed a calibration technique to quantify Au and Ti. The total mass measured across the size distribution was compared with certified values of ionic standards, acid digestion measurements of particulate Au, and gravimetric measurements of Ti. We also measured several control NPs: gold nanorods (AuNRs), gold nanocubes (AuNCs), AuNPs, and platinum coated AuNPs (Pt@AuNPs), to examine the effect of morphology and composition. The results demonstrate that DMA-ICP-MS can be used to accurately measure mass distributions of monodisperse NPs. However, DMA-ICP-MS measurements of polydisperse metal oxide NPs reproducibly and significantly measured more total mass than alternative batch measurements (i.e., acid digestion). Discussion on approaches for design and improved modeling to reduce the overestimation of HNP is included. Despite this issue, we demonstrate DMA-ICP-MS is a promising technique for further understanding of bimetallic HNPs by measuring calibrated mass distributions of multiple elements concurrently.

2. Materials and methods[2]

2.1. Chemicals

Sodium citrate dihydrate ($\geq$99%), oleylamine (70%), tetralin (97%), gold (III) chloride hydrate (99.999%), hexane ($\geq$97.0%), and

---

t-butylamine-borane complex (97%) were purchased from Sigma Aldrich (St. Louis, MO, USA). Optima grade nitric acid, optima grade hydrochloric acid, and methanol (99.9%) were purchased from Thermo Fisher (Waltham, MA, USA). 2-propanol (100%) was purchased from J.T. Baker (Phillipsburg, NJ, USA). Sodium 1-hexadecanesulfonate was purchased from TCI (Portland, OR, USA). Thiourea (99%) was purchased from Alfa Aesar (Haverhill, MA, USA). Samples were prepared using 18.2 MΩ cm deionized water (Model 2121AL, Aqua Solutions, Jasper, GA, USA).

2.2. Standards

2.2.1. Au ionic standard

VWR BDH Aristar (Radnor, PA, USA) 999 µg mL^{-1} ± 5 µg mL^{-1} Au in 2% (v/v) HNO$_3$ was used as a stock standard. Dilutions to 100 µg L^{-1} – 1000 µg L^{-1} were made with 378 mg L^{-1} citrate or 378 mg L^{-1} citrate and 0.1% (mass/mass solution, (mass thiourea) (mass solvent and thiourea)$^{-1}$, m/m) thiourea in Lo-bind microcentrifuge tubes.

2.2.2. Ti ionic standard

NIST SRM 3162a Ti standard solution was used as a stock standard for dilutions to 100 µg L^{-1} – 5000 µg L^{-1} in 378 mg L^{-1} citrate in Lo-bind microcentrifuge tubes. The certified concentration is 9.879 mg g^{-1} ± 0.019 mg g^{-1} in 10% nitric acid and 2% hydrofluoric acid.

2.2.3. Quality control AuNPs

QC1 is citrate stabilized, nominally 30 nm AuNPs obtained from Ted Pella. Total mass of dilutions was determined gravimetrically based on sp-ICP-MS measurements of the as purchased NP stock mass concentration: 47.4 µg g^{-1} ± 5.6 µg g^{-1}.

QC2 is citrate stabilized, nominally 60 nm AuNPs obtained from Ted Pella. Total mass of dilutions was determined gravimetrically based on sp-ICP-MS measurements of the as purchased NP stock mass concentration: 52.5 µg g^{-1} ± 5.7 µg g^{-1}.

2.3. Nanomaterials

Some properties of the various nanomaterials used to characterize the method are summarized in Table 1.

2.3.1. Gold nanorods (AuNRs)

Citrate stabilized AuNRs of three different geometries (peak absorbance 660 nm: 20 nm diameter and 55 nm length. Peak absorbance 800 nm: 10 nm diameter and 50 nm length. Peak absorbance 980 nm: 10 nm diameter and 60 nm length) were purchased from nanoComposix (San Diego, CA, USA).

2.3.2. Gold nanocubes (AuNCs)

Citrate stabilized AuNCs with 60 nm edge length were purchased from Nanopartz (Loveland, CO, USA).

2.3.3. Platinum coated gold nanoparticles (Pt@AuNPs)

30 nm AuNPs from Ted Pella were loaded with ionic platinum (Pt@AuNPs) by applying cisplatin solution to suspensions of polyethylene glycol-containing-dendron stabilized AuNPs.

2.3.4. Aluminum oxide NPs (Al$_2$O$_3$)

Aluminum oxide NPs (Cat. # 90–187,015) were purchased from Allied High Tech Products (Compton, CA, USA).

2.3.5. 10 nm AuNPs

Nominally 10 nm AuNPs were purchased from Ted Pella (Redding, CA, USA).

2.3.6. Titanium dioxide NPs (TiO$_2$; P25)

NIST SRM 1898 titanium dioxide NPs (also known as P25) were used.

2.4. Titania NPs coated with small AuNPs (Au@TiO$_2$)

AuNPs (4 nm) were synthesized (Peng et al., 2008) and adsorbed to larger titania NPs (Peng et al., 2008). Au@TiO$_2$ were then dried and heated before sonication to redisperse the HNPs in water.

2.4.1. Gold nanoparticle (AuNP, 4 nm) synthesis

Tetralin (10 mL), oleylamine (10 mL), HAuCl$_4$–3H$_2$O (50 mg) were mixed in a 100 mL round bottom flask heated at 40 °C while stirring. The solution turned orange. t-butylamine-borane complex (45 mg), tetralin (1 mL), and oleylamine (1 mL) were mixed in a small vial and bath sonicated. The reducing agent mixture was injected into the 100 mL round bottom flask solution and left for 1 h. The contents of the round bottom flask were transferred slowly to 200 mL isopropanol while stirring. Stirring was stopped after 10 min and the NPs were left for 12 h to precipitate. Supernatant (200 mL) was removed, and the remaining dispersion was transferred to centrifuge tubes. The AuNPs were redispersed in isopropanol, bath sonicated for 5 min, and then centrifuged at 6000 rcf for 5 min. The

Table 1
Physical characteristics of used standards and nanomaterials.

Material	Shape	Nominal size (Coefficient of variation)	Source
Supported bimetallic materials			
Au@TiO$_2$	Fractal	150 nm (50%)[a]	Synthesized following Cargnello et al., 2015
Al$_2$O$_3$	Fractal	70 nm (40%)[a]	Allied High Tech Products*
Pt@AuNPs	Sphere	30 nm (8%)[a]	Synthesized following Tan et al., 2018
NPs			
QC1	Sphere	30 nm (5%)[b]	Ted Pella*
QC2	Sphere	60 nm (7%)[b]	Ted Pella*
AuNRs	Rod	20 nm diameter (4%)[b], AR 2.75	NanoPartz*
AuNRs	Rod	10 nm diameter (4%)[b], AR 5	NanoPartz*
AuNRs	Rod	10 nm diameter (9%)[b], AR 6	NanoPartz*
AuNCs	Cube	60 nm (3%)[b]	NanoPartz*
Ionic Standards			
Au	–	–	VWR*
Ti	–	–	NIST

[a] Mode and CV of mass distribution measured by ES-DMA-ICP-MS.
[b] Mean and CV of number distribution measured by ES-DMA-CPC.

supernatant was removed, replaced with isopropanol, and repeated for three total cleaning cycles. After the final centrifugation, the supernatant was removed, and the final product was dispersed in 10 mL hexane (final concentration was approximately 2.5 mg mL^{-1}).

2.4.2. Adsorption

Sodium 1-hexadecanesulfonate (NaHDS, 5 mg) was bath sonicated for 5 min in methanol (1 mL). Calcined P25 (50 mg) was bath sonicated in hexane (12 mL) and NaHDS (625 μL). 4 nm AuNPs 1 μL–1000 μL were added and the dispersion was shaken vigorously. The dispersion was then centrifuged at 6000 rcf for 5 min. The supernatant was removed and the AuNP concentration in the supernatant was tested with UV–Vis (detailed below). Hexane (12 mL) was replaced, and the dispersion was centrifuged at 6000 rcf for 5 min. The process was repeated for three total cleaning cycles (add hexane, centrifuge, remove supernatant). After the third centrifugation the supernatant was removed, and the dispersion was air dried.

2.4.3. UV–Vis

UV–Vis absorbance measurements were made from 200 nm–800 nm to test the concentration of AuNPs left in the supernatant after adsorption relative to the stock concentration of AuNPs (Model Lambda 750, PerkinElmer, Waltham, MA, USA). A slight peak was detectable around 530 nm. The AuNPs in suspension were undetectable for samples with Au loading equal to or below 5E-3 mg AuNP per 1 mg P25.

2.4.4. Heat treatment

Dried Au@TiO$_2$ powder was smoothed with wax paper and transferred to a crucible for heating. The powder was heated at 500 °C for 1 min to remove adsorbed oleylamine (Cargnello et al., 2015).

2.4.5. Storage

After heating, any powder not used immediately was transferred to a parafilm sealed container and stored in a desiccator. Initial experiments with TEM found significant changes in absorbed AuNP size after 6 months when not stored properly.

2.4.6. Sonication

After sufficient heating and removal of the organic ligands, the Au@TiO$_2$ powder was dispersible in water. The Au@TiO$_2$ powder (10 mg, weighed on an analytical scale sensitive to 0.1 mg) was dispersed in 10 mL of 378 mg L^{-1} citrate in water and 30 W–50 W, based on the sample, were applied to the suspensions using a probe sonicator (Branson Ultrasonics, Brookfield, CT) equipped with a 0.5" horn. All suspensions were placed in ice baths to minimize sample degradation during sonication. Maximal dispersion of the metal oxide samples, defined by unchanging mass distributions observed with laser diffraction (Model: LA-950V2, Horiba, Kyoto, Japan), were found to apply at approximately 30 W at 80% duty cycle. Laser diffraction measurements demonstrated that most of the NP volume distribution reduced to the sub 200 nm size range consistent with previous TiO$_2$ samples (Taurozzi et al., 2013).

2.4.7. Au acid digestion

Sample powder (2 mg) was added to 7% (v/v) aqua regia (10 g) and left for 48 h. The digested sample was then diluted to approximately 10 μg L^{-1} Au in 1% (v/v) aqua regia with 0.1% (m/m) thiourea. The Au concentration was then determined by traditional ICP-MS measurements (Supplementary Materials) with comparison to an ionic standard calibration curve from 1 μg L^{-1} to 50 μg L^{-1}.

2.5. ES-DMA-ICP-MS instrumentation

The customized electrospray-DMA system used in this study has been described previously (Duelge et al., 2020). Briefly, the electrospray (ES, Model 3480, TSI, Shoreview, MN, USA) used an aerosol flow rate of 1 L min^{-1} air. The ES voltage was set to 3 kV with a resulting current of 200 nA–400 nA. The pressurized sample chamber was set to 26 kPa (3.7 psi). The samples were sprayed through a 40 μm inner diameter fused silica capillary. The aerosol was charged to a bipolar distribution by a Po-210 alpha-emitter (Model P-2042, TSI). The DMA (Model 3081, TSI) selected positively charged NPs with a narrow mobility range. A custom LabVIEW (National Instruments, Austin, TX, USA) program was used to control the high voltage power supply (Model 205B-10R, Spellman, Hauppauge, NY, USA). The voltage ranged from 0 V–4000 V, limited by the electrical breakdown of argon (Ar). A mass flow controller (Model 1480A01334CS1BM, MKS Instruments, Andover, MA, USA) was used to set a variety of sheath flows, from 4 L min^{-1} to 10 L min^{-1} Ar, though the most common sheath flow was 10 L min^{-1} Ar. The measurable NP size range varies with the sheath flow, from 10 nm–150 nm at 10 L min^{-1} Ar, to 10 nm–230 nm at 4 L min^{-1} Ar. The NPs selected by the DMA then passed through a custom gas exchange device (GED) described previously (Elzey et al., 2013). The size selected aerosol travelled through a region surrounded by a porous Al$_2$O$_3$·SiO$_2$ membrane contained in a glass tube. Ar and air traversed the membrane by diffusion with minimal loss of NPs, as demonstrated previously with DMA-GED-CPC measurements compared to DMA-CPC measurements (Elzey et al., 2013). A 3 L min^{-1} Ar flow outside the membrane travelled in the opposite direction compared to the aerosol flow for improved exchange.

To aerosolize NPs, generally ES or nebulization are used. In this case we chose to use ES due to the low sample volume requirements and the monodisperse droplet distribution (coefficient of variation, CV, less than 15%, the standard deviation of the number distribution divided by the number average size) that exits the spray chamber. HNP catalysts are currently produced in small quantities and the catalytically active metal mass fraction tends to be very low. Additionally, the calibration with an ionic standard is easier with monodisperse droplets. The size of the droplets that exit the spray chamber determine the resulting NP size of dried ionic standard. Spraying ionic standard with monodisperse droplets concentrates most of the mass within a narrow size range that can be measured rapidly and allows for easy identification of spray issues. However, a limitation of ES is that the solution must be conductive. Additionally, if a non-volatile salt is used, the mobility diameter of NPs can increase during drying of the droplets. Measurement accuracy also requires a Taylor cone to produce consistent droplets that contain ideally single NPs. The glass capillary of the ES can be a severe limitation to reproducible measurements. Both NPs and ions tend to adsorb to the capillary to some extent, but more importantly, NP adsorption leads to reductions in capillary flow and eventually clogs the capillary. For this reason, we cleaned the capillary with ethanol and buffer between NP measurements and used different capillaries for NPs and ionic solutions.

Elemental quantification measurements were made with ICP-MS, (Agilent 7900, Santa Clara, CA, USA) in batch mode and hyphenated to the aerosolized analytes outlined in Fig. 1. The design for introduction of Ar after the ES at the appropriate rates for ICP-MS can be found elsewhere (Elzey et al., 2013). Time resolved analysis measurements of ^{197}Au and ^{47}Ti were made with a 1 s integration time. ^{47}Ti was chosen due to linearity of response over the concentration ranges examined and fewer polyatomic and isobaric interferences than ^{48}Ti. The ICP-MS was calibrated and tuned daily in batch mode to optimize the ^{197}Au intensity before hyphenation with DMA. Additional ports to control make up and dilution Ar flows at the ICP-MS inlet were examined to evaluate ^{197}Au intensity repeatability for both ionic standards and NPs. The repeatability of signal intensities for ionic calibration standards were checked daily to ensure data comparability for all measurements.

Measurements to determine Ti and Au mass distributions were made of various sized NPs from different vendors. The ICP-MS operated continuously while the DMA stepped through a series of voltages (10 V–4000 V) corresponding to specific mobility diameters depending on the sheath flow (10 nm–150 nm for 10 L min^{-1} sheath flow). The DMA remained at each voltage for 30 s, allowing for multiple measurements by the ICP-MS per selected mobility diameter. The average ICP-MS response was determined for each diameter and the data was converted from a time distribution to a diameter distribution. The transit time between the DMA and the ICP-MS (16 s) was used to determine the start of the first 30 s interval, corresponding to the smallest NP size. The ICP-MS data for this and each subsequent 30 s interval was averaged and associated with the corresponding NP size. The data were corrected for background noise, and the mass distribution post-DMA was related to the mass distribution pre-DMA by the DMA transfer function and the charging probability at each diameter (because only charged NPs can transverse the DMA). Finally, the peak area of the mass distribution was integrated and plotted against the known total mass concentration from the certified values of ionic standards, acid digestion measurements of particulate Au, and gravimetric measurements of Ti. The gravimetric analysis of Ti was based on the weighed Au@TiO$_2$ powder, corrected for the mass fraction of Au and the contribution from oxygen to the total mass (only Ti is detected
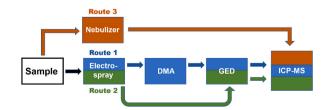

Fig. 1. *Method schematic to visualize the differences in the modular components for each type of experiment compared in the current work. The different colors represent each configuration that was used. DMA is differential mobility analyzer, GED is gas exchange device, and ICP-MS is inductively coupled plasma mass spectrometer. (For interpretation of the references to color in this figure legend, the reader is referred to the Web version of this article.)*

by the ICP-MS). Some alternative methodologies were used to troubleshoot the method, and these are detailed in the Supplementary Material. A schematic of the various methods is given in Fig. 1.

2.6. Calculations

The peak mobility (Z_{p1}) of a charged NP exiting the DMA is obtained using the following equation:

$$Z_{p1} = \frac{q_s \ln(r_2/r_1)}{2\pi VL} \tag{1}$$

where V is the electrical potential, q_s the sheath flow, L is the length of the classification region, and r_1 and r_2 are the inner and outer electrode radii. The term "peak" refers to the mode of the DMA transfer function for a given value of the voltage and flow rates. The subscript p refers to NP and 1 refers to the peak value.

A key advantage of the DMA is that it has a quantified transfer function. This is essential for determining the size distribution of the aerosol entering the DMA from measurements of the aerosol exiting the DMA. Another advantage is that one can obtain high resolution mobility measurements by using a low aerosol flow and a high sheath flow ($\Delta Z_p/Z_p = 0.1$ for a flow ratio of 10).

The sphere equivalent mobility diameter distribution is of interest rather than the mobility distribution. For singly charged NPs, the diameter (D_p) is related to the mobility via the following implicit equation:

$$\frac{D_p}{C_c} = \frac{ne}{3\pi\mu Z_p} \tag{2}$$

n is the quantity of elementary charges on the NP, e is the elementary charge, μ the viscosity, and C_c the Cunningham slip correction factor.

$$C_c = 1 + K_n(\alpha + \beta(\exp(-\gamma / K_n))) \tag{3}$$

The parameter K_n is the Knudsen number, $2\lambda/D_p$, where λ is the mean free path, and α, β, and γ are empirical constants. In this case we use the values $\alpha = 1.165$, $\beta = 0.483$, and $\gamma = 0.997$ (Kim et al., 2005).

Knutson and Whitby derived an equation relating the NP concentration at the DMA exit, $N_{CPC}(D_p)$, to an integral involving the DMA transfer function and the number size distribution (Knutson & Whitby, 1975). For the common condition that the aerosol distribution is broad compared to the transfer function, the following relationship is obtained:

$$\frac{dN(D_p)}{dD_p} = \frac{N_{CPC}(D_p)B(D_p)}{\varepsilon P(D_p)} \tag{4}$$

where $dN(D_p)$ is the number concentration of NPs with diameters between D_p and $D_p + dD_p$. The proportionality constants are the singly charged fraction, $P(D_p)$ (Wiedensohler, 1988), which accounts for the difference between the bipolar charge distribution at the inlet and the singly charged NPs at the outlet, the aerosol-to-sheath flow ratio, ε, which relates to the DMA sizing resolution, and the function $B(D_p)$, which arises from the transformation from a mobility distribution to a diameter distribution (Mulholland et al., 2006). The derivation of Equation (4) is given in Appendix 1.

We are interested in the mass distribution, $\frac{dM(D_p)}{dD_p}$, which is related to the number distribution, $\frac{dN(D_p)}{dD_p}$, via the following formula for spherical NPs:

$$\frac{dM(D_p)}{dD_p} = \frac{1}{6}\pi D_p^3 \rho \frac{dN(D_p)}{dD_p} \tag{5}$$

where ρ is the NP density. Multiplying both sides of Equation (4) by $\frac{1}{6}\pi D_p^3 \rho$, one obtains:

$$\frac{dM(D_p)}{dD_p} = \frac{M_{det}(D_p)B(D_p)}{\varepsilon P(D_p)} \tag{6}$$

where M_{det} is the mass concentration of the outlet aerosol measured by a mass detector such as a filter/gravimetric weighing, a tapered element microbalance, or ICP-MS. ICP-MS, the method of interest here, has the advantage of having a much higher sensitivity to small masses compared to other methods. One of the major interests is in computing the total mass concentration: M_T. This is obtained by summing over the number of size bins (m) which is determined by the number of voltage steps in the measurement:

$$M_T = \sum_{i=1}^{m} \frac{\Delta M_i}{\Delta D_{p,i}} \Delta D_{p,i} = \sum_{i=1}^{m} \Delta M_i \tag{7}$$

There are several assumptions in the derivation of Equation (4). NP diffusion has not been included and more recent charging theory (Gopalakrishnan et al., 2013) indicates that the Wiedensohler regression underpredicts the charging for diameters less than 100 nm. A calculation of the total mass (Equation (7)) for Au@TiO$_2$ HNPs was 5% lower using recent charging theory compared to the Wiedensohler regression. NP losses downstream of the DMA have not been treated; however, the losses may be similar for the

calibration NPs and the bimetallic HNPs.

One case of interest is a bimetallic catalyst NP such as a Ti NP with small AuNPs adsorbed on the surface. In this case we are interested in the mass distribution of Au, dM_{Au}/dD_p, where the detector response is only for Au. In this case the Au mass is only a small fraction of the total mass of the NP. The corresponding equation for the relationship between the mass distribution and the ICP-MS measurements for Au is:

$$\frac{dM_{Au}(D_p)}{dD_p} = \frac{\left[M_{det, Au}(D_p) - M_{background,Au}\right]B(D_p)}{\varepsilon P(D_p)} \tag{8}$$

The ICP-MS signal intensity in counts per second (cps) is averaged for each period corresponding to different mobility diameters. The ICP-MS signal intensity at no applied voltage is subtracted from each point to correct for the background signal, $M_{background,Au}$.

3. Results

Determination of Au concentration on TiO_2 NPs provides the baseline for observed responses for supported metal systems in reactivity, optical response, and other applied performance metrics. To determine the relationship between metal loading of uniform NPs and performance, accurate quantification of metal amounts or elemental ratios of metal and scaffold (i.e., Au and Ti) is necessary. Here, the elemental response for different metal states, primary NPs, ions, and supported metal NPs are examined with hyphenated ES-DMA-ICP-MS to develop improved methods for characterizing multi-component metal NPs. Although previous work has suggested accurate quantification was straightforward for all metal matter forms, no in-depth study has investigated possible sources of error that could be present for accurate metallic ratios or absolute quantification (Elzey et al., 2013; Hess et al., 2016).

Calibration curves for Au and Ti are shown in Figs. 2 and 3, respectively. The curves plot the mass concentration, [M], (from the certified concentration of the ionic standard, acid digestion measurements for QC1, QC2, AuNCs, AuNRs, Pt@AuNPs, and Au@TiO₂, or gravimetric analysis for TiO₂ samples) versus the integrated peak area of the ES-DMA-ICP-MS response, M_T. Fig. 2 indicates two response regimes: one for the Au ionic standard and monodisperse AuNPs (CV less than 15%), and a second for polydisperse Au@TiO₂ (CV greater than 30%). The inset of Fig. 2 exhibits the linear relationship between [Au] and $M_{T,Au}$. The slopes of the linear plot clearly exhibit the divergence in the fitted calibration curves for Au@TiO₂ and the calibration candidate Au samples. At the concentration for the 30 nm AuNPs, QC1: [Au] = 4700 µg L⁻¹, the $M_{T,Au}$ for the ionic standard blue line is 40% less than the Au@TiO₂ black line. For all other figures, we presented the data in logarithmic scale to present the entire concentration range evaluated.

Fig. 3 presents the difference between the Ti ionic standard and the pristine TiO₂ NPs (no Au). The ES-DMA-ICP-MS response is significantly higher for Au@TiO₂ and TiO₂ than the ionic standards or monodisperse nanomaterials. This difference is consistent for Au and Ti. Fig. 2 demonstrates the agreement between the ES-DMA-ICP-MS calculated M_T and the mass concentration for the Au ionic
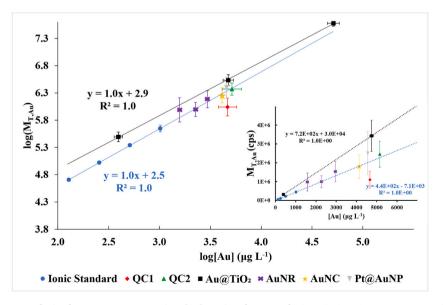

Fig. 2. *Au calibration curves plotting known mass concentration, [Au], against the summed ES-DMA-ICP-MS response, $M_{T,Au}$. The axes are presented logarithmically in the main panel to visually represent the wide range of concentrations measured. The linear scales in the inset demonstrate the diverging response of each Au calibration candidate measured against the Au@TiO₂. For the concentration at QC1: [Au] = 4700 µg L⁻¹, the difference in $M_{T,Au}$ is 40% between the diverging blue and black regression lines, where all data points were used in the regression analysis for both panels. The blue circles are the Au ionic standard, black squares are Au@TiO₂, red diamonds are QC1, green triangles are QC2, purple X are AuNRs, yellow stars are AuNCs, and gray inverted triangles are Pt@AuNPs. Y-axis error bars represent one standard deviation of measurements from several days (number of measurements n = 3). The x-axis error bars indicate one standard deviation and propagated uncertainty of the concentration (based on dilutions from the stock). (For interpretation of the references to color in this figure legend, the reader is referred to the Web version of this article.)*
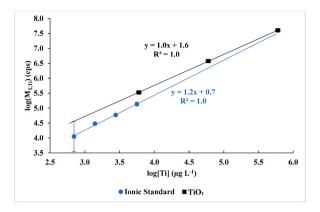
Fig. 3. *Ti calibration curve plotting known mass concentration against the summed ES-DMA-ICP-MS response. The axes are scaled logarithmically due to the wide range of concentrations measured. The blue circles are the Ti ionic standard, and the black squares are particulate TiO$_2$ samples (no Au). Y-axis error bars represent one standard deviation of measurements from several days (number of measurements n = 3). The x-axis error bars indicate one standard deviation and propagated uncertainty of the concentration (based on dilutions from the stock). (For interpretation of the references to color in this figure legend, the reader is referred to the Web version of this article.)*

standard and AuNPs: QC1 and QC2, which indicates that the ionic and AuNP behavior through the ES is consistent. The agreement demonstrates the method is applicable to metallic NPs of different sizes and over a broad concentration range. The data indicates that accurate measurements of Au@TiO$_2$ are a more difficult challenge than ionic samples or monodisperse NPs.

Figs. 4 and 5 plot the mass concentration (from the certified concentration of the ionic standard and acid digestion measurements for Au@TiO$_2$) versus the ICP-MS response. The difference between the Au ionic standard and Au@TiO$_2$ when the DMA is not used (the ES is connected directly to the GED-ICP-MS, green track in Fig. 1) is shown in Fig. 4. The data show a higher ^{197}Au signal for Au@TiO$_2$ (black squares) compared to ionic Au (blue circles). The comparison of Figs. 2 and 4 suggests a significant portion of this bias does not derive from the DMA. Fig. 5 shows that this bias was not detected when the same measurements were made with a nebulizer instead of the ES and GED. The ideal behavior, if the nebulizer works as intended, is that the ionic standard and Au@TiO$_2$ fall on a single line. In Fig. 5, the observed behavior is closer to this expectation than previous figures. There is a minor difference, with higher response for the ionic standard relative to Au@TiO$_2$, consistent with NP loss prior to measurement (visible precipitation in the plastic tubing used for pneumatic pump). This contrast between Figs. 4 and 5 suggests the ES and/or the GED contribute to the higher response for Au@TiO$_2$. Additionally, difference matrices were used for the ionic standards in Figs. 4 and 5. The ideal matrix for ionic Au is aqua regia with thiourea, but this is not compatible with the spray chamber of the ES. Both measurements were made with the most stable matrix available for the given spray source, but some differences in ICP-MS response may derive from this difference.

Additional digestion experiments were conducted to examine whether the ionic standard and digested NP solutions behaved similarly when measured with ES-DMA-ICP-MS (results not shown). The NPs were digested for increasingly long periods of time, up to 48 h, but demonstrated no change in Au concentration, suggesting that complete NP digestion was achieved. The linear fit to the blue, green, and red points in Fig. 2 demonstrate that the ES-DMA-ICP-MS measurements of total Au mass of QC1 and QC2 are consistent with the ES-DMA-ICP-MS measurements of total Au mass of the ionic standard. Based on this agreement, the ES-DMA-ICP-MS
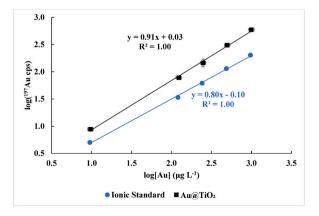

Fig. 4. ES-ICP-MS (no DMA) measurements of Au ionic standard diluted in citrate thiourea buffer (blue circles) and Au@TiO$_2$ (black squares). The axes are scaled logarithmically for convenient comparison to other figures. Y-axis error bars represent one standard deviation of triplicate measurements. The x-axis error bars indicate one standard deviation and propagated uncertainty of the concentration (based on dilutions from the stock). (For interpretation of the references to color in this figure legend, the reader is referred to the Web version of this article.)
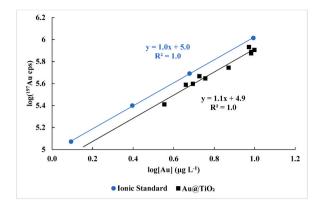
Fig. 5. Nebulizer-ICP-MS (no DMA) measurements of Au ionic standard diluted in 1% (v/v) aqua regia and 0.1% (m/m) thiourea (blue circles) and Au@TiO$_2$ diluted in 378 mg L^{-1} citrate buffer (black squares). The axes are scaled logarithmically for convenient comparison to other figures. (For interpretation of the references to color in this figure legend, the reader is referred to the Web version of this article.)

measurement was able to determine representative mass distributions of QC1 and QC2 in Fig. 6. ES-DMA-ICP-MS measurements of QC1 and QC 2 were acquired at a ten-fold dilution, but the values of M_T were scaled proportionally to the dilution such that the figure represents the original stock concentration.

Possible sources for the differences between the ionic standard and Au@TiO$_2$ derived from the DMA were investigated, such as the effect of NP shape and multiple charging. In Fig. 2, monodisperse particulate Au of various shapes (rods and cubes) were compared to the results for the ionic standard and Au@TiO$_2$. The rods and cubes tended to agree with the ionic standard more than Au@TiO$_2$, suggesting these shapes are not the source of the error. The Au@TiO$_2$ NPs are fractals, however, and this particular shape could be the source of error with the quantification.

The analysis of the DMA used assumed that there are only singly charged NPs. However, it is possible that there are doubly and triply charged NPs as well. This can impact accurate quantification, because a triply charged 310 nm NP has roughly the same mobility as a 190 nm doubly charged NP and a 150 nm singly charged NP. To investigate the effects of multiple charging, additional experiments to detect the entire mass range generated from the ES were run to examine if a significant mass fraction was above the upper size limit for the classifier. In Fig. 7A, the DMA sheath flow was decreased to 4 L min^{-1} so the largest possible size range for the current instrument setup, 10 nm–230 nm, was measured. A linear fit of the slope from 160 nm–230 nm resulted in an intercept near 310 nm, which was used as the largest NP size (all singly charged) for the charge correction calculation using Equations (25) and (30) (see Appendix 2). This largest NP size was consistent with ES-DMA-ICP-MS measurements made with an impactor that found minimal contribution to the total mass above 300 nm.

Fig. 7B illustrates the significant decrease in calculated mass from 50 nm–190 nm due to the correction of the convolution of larger doubly and triply charged NPs with smaller singly charged NPs. The total mass from 10 nm–150 nm was reduced by 34% with the correction for doubly charged NPs and was reduced by 37% with the correction for doubly and triply charged NPs. The same correction was applied to calculate the calibrated mass distributions of Au and Ti for Au@TiO$_2$ NPs in Fig. 7C. This is a sample with low Au loading, near the limit of detection for the ES-DMA-ICP-MS measurement, at 4.2×10^{-4} mass fraction. The percent error for the agreement with the ionic standard calibration curve is presented in Table 2. The charge correction improved the error for polydisperse Au@TiO$_2$ while minimally impacting the monodisperse AuNPs and demonstrates the approach is rational.
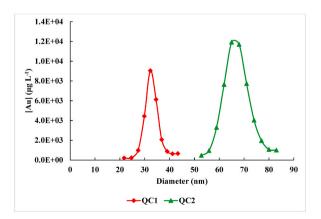

Fig. 6. Average calibrated mass distribution of QC1 (red diamonds: 32 nm mode) and QC2 (green triangles: 66 nm mode). (For interpretation of the references to color in this figure legend, the reader is referred to the Web version of this article.)
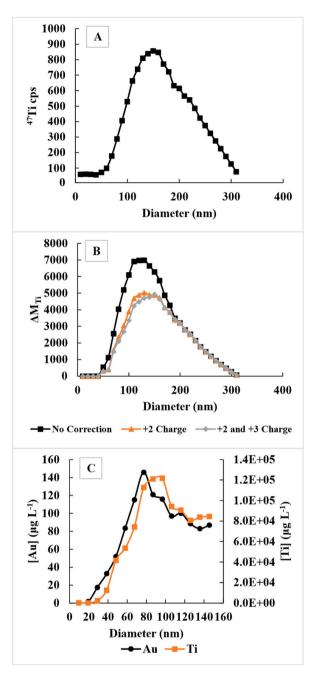
Fig. 7. A. The modified ES-DMA-ICP-MS full scan of ^{47}Ti for Au@TiO$_2$. The measurement was made from 10 nm–230 nm and a linear fit was continued from 240 nm–310 nm. B. The Ti uncalibrated mass distribution of Au@TiO$_2$ assuming all NPs are singly charged (black squares), correcting for doubly charged NPs (orange triangles), and correcting for doubly and triply charged NPs (gray diamonds). C. The calibrated mass distribution of Au@TiO$_2$ with Au mass fraction (4.2E-4) corrected for +2 and + 3 charges. The black circles indicate the Au concentration, and the orange squares indicate the Ti concentration. (For interpretation of the references to color in this figure legend, the reader is referred to the Web version of this article.)

4. Discussion

To accurately measure metallic clusters present on supported catalysts, or more generally, accurately determine mass ratios of specific subpopulations of species in a mixture, the size, distribution, and the relative mass fractions of species in the sample must be determined. Hyphenated ES-DMA-ICP-MS measurements meet the requirements to provide higher resolved mass distributions across the NP population, which can be a powerful tool in conjunction with electron microscopy and other measurements for more complete

material characterization. However, requirements for producing stable, monodisperse droplets to achieve the accuracy necessary to be used as a research tool for material development and analysis must be identified. Here we provide a more complete investigation of the uncertainties and challenges associated with calibrating and accurately quantifying masses in supported metal systems that have not been rigorously evaluated until this work.

The ES requirements are why the measured concentration calibration ranges of the ionic standard and Au@TiO$_2$ were different (x-axes of Figs. 2 and 3). Increasing the concentration of Au or Ti ions increases the conductivity above the range that can be stabilized by this model ES. Our efforts were focused on assessing the mass distributions at the limits of size detection, size distribution range, and smallest cluster populations that could be detected if single masses were selected. The primary discussion will focus on the mass distribution at the size limit of detection and the size distribution range.

Significant efforts were made to determine the cause of the observed discrepancy in response between Au@TiO$_2$ and the ionic standard and identify the major sources of possible error for other applied material systems. The primary evidence we present that the system can be accurately calculated and validated is the consistency between ES-DMA-ICP-MS calculated M_T and the mass concentration for the ionic and pure component NP suspensions. Because those measurements agree, we could conclude that the uniform ES droplets of well mixed ion solutions (that subsequently evaporate and form salt NPs) behave the same as sprayed metal and metal oxide NP suspensions. The agreement of the pure component measurements then allowed our investigation of overestimation to be centered on the individual contributions of the instrument components on the measurement of the HNPs and metal oxide support NPs.

Our initial hypothesis for the observed overestimation was the presence of large diameter Au@TiO$_2$ aggregates that would be undetected by the DMA above the 230 nm upper limit. Multiple issues with the presence of NP populations above 150 nm exist for both DMA and ICP-MS, which include lower elemental sensitivity associated with lower sheath flow of Ar into the plasma and charge capacity of the metal oxide NP agglomerates, for example. Larger NPs have a higher probability to have multiple charges than smaller NPs and multiply charged large NPs will exit the DMA at the same voltage as singly charged smaller NPs (ISO, 2020). The excess mass may be due to the assumption that we are only detecting singly charged smaller NPs, because overcounting multiply charged species would contribute to the overestimation. To test the hypothesis of an unmeasured population, samples were run with and without an impactor that removes aggregates above 300 nm. Although the efficiency of the impactor does allow some larger NPs to pass through, we used it as a qualitative assessment to see if the measured $M_{T,Ti}$ and $M_{T,Au}$ were affected within the uncertainty of the measurements. The inclusion of the impactor did not change the total mass of Au or Ti that was measured, indicating that there was not a population of large aggregates present in quantities above the limit of detection for the ICP-MS; thus, this is not the source of the overestimation.

The agreement between the ionic standard and the AuNPs led to questions about their similar behavior within the hyphenated ES-DMA-ICP-MS system and the contrasting differences to the metal oxide and HNP systems. Both ionic and AuNP species ostensibly traverse the DMA in the form of monodisperse, semi-spherical NPs, and the ionic distribution is assumed to be homogeneous (i.e., ion concentration to linearly scale with salt NP size). The Au@TiO$_2$ HNPs, in contrast, are polydisperse and fractal. An investigation to examine size, shape, and homogeneity of the samples was conducted.

The first examination was conducted on the ionic standards. The measurements of the ionic standards were generally done in a narrow size range due to the monodisperse droplet distribution that exits the ES spray chamber. This decision was based on our experience and expertise with conventional DMA-CPC number concentration measurements. Though no significant secondary population exists in the number distribution, the same may not be true for the mass distribution measured by ES-DMA-ICP-MS. It is possible that a small number of large diameter NPs contain a significant portion of the total mass of the ionic standard and contribute to an underestimation of the mass. To test this, we measured the ionic standard over the entire measurable size range (Figure S-2), from 10 nm–150 nm, but detected no significant difference from the narrower measurements (16 nm–40 nm). This suggests the measurement of the peak is sufficient, metal ions were entrained and detected in salt species consistently, and the method to determine mass was sufficient. For the pure component Au systems that generally agreed with the ionic standard, the anisotropy, small variations

Table 2

Au and Ti ES-DMA-ICP-MS total mass values from 10 nm–150 nm with and without the correction for multiple charges. The percent error indicates the difference between the expected M_T from the ionic standard calibration linear fit and the measured M_T.

Sample	Measurement	No Correction	+2 Charge Correction	+2 and + 3 Charge Correction
Au@TiO$_2$	Au M_T	3.79E7	2.84E7	2.74E7
5.2E-2	Au % Error	67	25	21
Au Mass	Ti M_T	5.87E7	4.25E7	4.07E7
Fraction	Ti % Error	127	64	57
Au@TiO$_2$	Au M_T	3.43E6	2.71E6	2.63E6
5.1E-3	Au % Error	64	30	26
Au Mass	Ti M_T	6.65E7	5.02E7	4.86E7
Fraction	Ti % Error	153	91	85
Au@TiO$_2$	Au M_T	3.12E5	2.34E5	2.25E5
4.2E-4	Au % Error	83	39	34
Au Mass	Ti M_T	6.01E7	4.44E7	4.27E7
Fraction	Ti % Error	129	69	63
QC1	Au M_T	1.11E7	1.10E7	1.10E7
	Au % Error	−47	−47	−47
QC2	Au M_T	2.29E7	2.27E7	2.27E7
	Au % Error	−1	−2	−2

in shape or mobility diameter, and composition of metallic state decorating the surface (in the case of Pt@AuNPs) were not factors that contributed to uncertainty of the same magnitude as the discrepancies observed in Fig. 2 between pure components/ions and Au@TiO$_2$.

Because TiO$_2$ exhibits the diverging overestimation in the absence of Au (Fig. 3), measurements of Au clusters on Al$_2$O$_3$ were made to test whether overestimation was specific to TiO$_2$ or could be more generally applicable to metal oxide supports. The Au@Al$_2$O$_3$ also showed higher ES-DMA-ICP-MS response than the ionic standard (Figure S-3), indicating that the effect is a general characteristic of metal oxide supports, which has broad implications for the use the hyphenated system for large number of fields similar material classes. Both metal oxides had broad distributions, but the modes differed, as shown in Figure S-4.

Although we identified the metal oxide support to be one contribution to the overestimation, the contribution of the Au or more generally the size of an active component on the support might also introduce uncertainty in quantifying the relative elemental ratios across the size distribution. To test this hypothesis, we loaded larger AuNPs that could individually be observed with ICP-MS onto titania. The contribution from larger AuNPs did not improve the agreement of the ionic and Au@TiO$_2$ on a scale that suggested underestimation of Au was a primary contributing factor to the observed differences (Figure S-5), i.e., the size of the Au cluster is not miscounted in the ICP-MS due to detection limits related to the Au concentration present per metal oxide NP.

As stated previously, the clear physical distinctions between Au@TiO$_2$ and the ionic standard are the NP shapes and size distributions. Both the dried ionic standard NPs and the AuNPs are nearly spherical and have a narrow distribution with a half width at half max on the order of 5 nm. The metal oxides used as scaffolds have an agglomerate morphology with primary spherules on the order of 20 nm–40 nm and have a broad range of mobility sizes with a half width at half max on the order of 70 nm for a 150 nm mass mode diameter. A possible explanation is that the charging efficiency of the metal oxides is higher than the corresponding efficiency for the pure metal, a hypothesis that has not been previously reported or demonstrated to the best of our knowledge.

A likely DMA related source of the overcounting of metal oxide NPs is multiple charging, as broad distributions could have large overlap between various charge states, while monodisperse solutions have more defined separations between charge states. Equation (2) demonstrates the inverse relationship between mobility (Z_p) and diameter (D_p) that is complicated by different charge states (n). To investigate this effect, we measured the widest size range possible with the current configuration: 10 nm–230 nm and used the data to extrapolate a full ES-DMA-ICP-MS measurement from baseline to baseline (Fig. 7A). This distribution is assumed to be representative of other measurements made at different flow ratios that allow for more sensitive detection by the ICP-MS. The charge correction assumes the largest NPs are 310 nm, meaning the mass detected at 310 nm corresponds only to singly charged 310 nm NPs. From this starting point, the proportion of doubly and triply charged NPs are calculated for each step and are corrected at the smaller diameter that corresponds to a singly charged NP with the same mobility. The correction shown in Fig. 7B was applied to all other Au@TiO$_2$ measurements. Fig. 7C shows the mass distribution of Au@TiO$_2$ with this correction, which can be used to determine the relative mass concentration of Au and Ti across the size distribution. The charge correction improved the agreement between the ionic standard and Au@TiO$_2$ but did not completely bridge the difference. Table 2 demonstrates the improved agreement between the ionic standards and Au@TiO$_2$ when multiple charging is considered. However, the method is still overcounting these HNPs, as the results in Table 2 only include the mass between 10 nm–150 nm and a significant portion of the total mass is expected at larger sizes. As a result, a percent error of approximately −60% is expected for proper agreement between the ionic standard and Au@TiO$_2$. The measurement is still overcounting by about a factor of 3–5, as the measured percent errors range from 21%–34% for Au and 57%–85% for Ti. Additional work is necessary for refining the model to improve accuracy, but general correction factors can be applied for reproducible overcounting of well controlled systems, such as the Au@TiO$_2$ HNPs used here, and widely implemented into applied research.

Identification of the other major sources for the overestimation, counting, or refining the charge modelling through improved data on the charge distribution on metal oxides formed in ES are necessary for further improved accuracy. However, our work identified a major source of error in quantification of active supported catalysts that was previously unreported and has broad implications for numerous scientific fields that rely on NP number calculations and mass determination of multiple component systems. Further developments can be made on similar systems with experimental designs that incorporate different DMA geometries or a more efficient GED such that the DMA sheath flow could use air instead of Ar to sample agglomerates larger than 150 nm. Solving this analytical challenge provides a general method for more accurate determination of the active NP distribution across the entire population. The current method can be used to detect preferential Au adsorption at different titania sizes, which could be caused by different preparation methods. Here, the mass ratio of Au-to-Ti is constant across the distribution with small variations likely due to the low concentration of Au, but synthesis modifications could change the distribution based on design needs. Furthermore, ES-DMA-ICP-MS is a tool that should help to elucidate differences of key NP features of existing and emerging materials, such as catalytic activity, between batches that were intended to be nominally equivalent and eventually accelerate design. The current development of appropriate calibration procedures allows immediate implementation for examining a broad class of metal supported HNPs being used in optical, catalytic, and other applications.

5. Conclusion

We made improvements on a universal calibration method for ES-DMA-ICP-MS measurements. The calibration efforts used ionic standards for the elements of interest and can detect multiple elements simultaneously, which is advantageous for HNPs like those used for catalyst applications. We identified previously unreported issues with overcounting for metal oxide supports that have broad implications for the scientific community. Thorough investigation of possible sources of uncertainty for quantification identified NP charging and the ES process as major contributions affecting mass distribution measurements. The correction for +2 and + 3 charged NPs improved the agreement between the ionic standard and metal oxide NPs; the total mass of TiO$_2$ was reduced by 34% with the +2

charge correction and 37% with the +2 and + 3 charge correction. We also demonstrated that this was consistent with other similar crystal size oxide supports. Because metal oxides are ubiquitous in applied systems, our work identifies a major source of error and provides a solution for generating reproducible accuracy for determining mass ratios across heterogeneous size distributions. We demonstrated this capability to be used to investigate the synthetic parameter space to control loading across each NP size population based on application need. More generally, ES-DMA-ICP-MS is a powerful tool that can rapidly average thousands of NPs and provide statistically meaningful data for material classes that have generally been limited to more limited sampling alternatives, such as electron microscopy.

Declaration of competing interest

The authors declare that they have no known competing financial interests or personal relationships that could have appeared to influence the work reported in this paper.

Acknowledgements:

Appendix A. Supplementary data

Supplementary data to this article can be found online at https://doi.org/10.1016/j.jaerosci.2022.106031.

Appendix 1

The derivation of Equation (4) is similar to that given previously (Mulholland et al., 2006). The mobility, Z_p, is determined by the balance of the drag force and the electrostatic force.

$$Z_p = \frac{neC_c(D_p)}{3\pi\mu D_p} \tag{9}$$

where n is the number of charges, e is the elementary charge, C_c is the Cunningham slip correction factor, μ is the viscosity of the gas, and D_p is the mobility diameter:

$$C_c = 1 + K_n(\alpha + \beta(\exp(-\gamma / K_n))) \tag{10}$$

where α, β, and γ are empirical constants for the slip correction.

Knutson and Whitby derived an expression for the number flux of NPs exiting the DMA at voltage V involving an integral over the product of the DMA transfer function Ω and the mobility probability distribution function (Knutson & Whitby, 1975). It is convenient for our application to express this equation in terms of the number concentration of charged aerosol, $N_{CPC}(V)$ exiting the DMA, which is the concentration measured by the CPC, and the number distribution of the charged aerosol leaving the DMA, $F_1(Z_p) = dN_1/dZ_p$, where $F_1(Z_p)dZ_p$ is equal to the number concentration of charged NPs with mobility between Z_p and $Z_p + dZ_p$.

$$N_{cpc}(V) = \int_0^\infty \Omega(Z_p \cdot V)F_1(Z_p)dZ_p \tag{11}$$

This equation applies to the case that there is at most one charge on each NP. The transfer function Ω for the DMA operating at voltage V is defined as the probability that a charged NP entering the DMA with electric mobility Z_p will leave through the sampling slit. The transfer function has a triangular shape with a peak value of 1 and, for a perfectly monodisperse aerosol, all the aerosol entering the DMA exits through the slit in the center electrode for the voltage corresponding to the peak in the transfer function. The value of the mobility at the peak in the transfer function at voltage V is given by:

$$Z_{p1} = \frac{q_s \ln(r_2/r_1)}{2\pi LV} \tag{12}$$

The ratio of the full width of Ω at half maximum divided by the peak value is given by:

$$\frac{FWHM}{Z_{p1}} = \frac{q_a}{q_s} = \varepsilon \tag{13}$$

where q_s and q_a are the sheath and aerosol flow rates.

Our primary interest is in obtaining the diameter size distribution, $G(D_p) = dN/dD_p$, where $G(D_p)dD_p$ is equal to the number of NPs per cm^3, charged and uncharged, entering the DMA with diameter between D_p and $D_p + dD_p$. Via the chain rule of derivatives and the difference between charged number concentration and total number concentration we obtain the following:

$$F_1(Z_p) = \frac{dN_1}{dZ_p} = P(D_p)\frac{dN}{dZ_p} = P(D_p)\frac{dN}{dD_p}\frac{dD_p}{dZ_p} = P(D_p)G(D_p)\frac{dD_p}{dZ_p} \tag{14}$$

The quantity $P(D_p)$ is the probability that a NP with diameter D_p carries one elementary unit of charge. From Equations (1) and (4), we obtain:

$$N_{cpc}(V) = \int_0^\infty \Omega(Z_p \cdot V) \ G(D_p(Z_p))P(D_p(Z_p))|dD_p / dZ_p|dZ_p \tag{15}$$

The absolute value of the derivative in Equation (15) reflects the fact that $F(Z_p)$ and $G(D_p)$ are positive definite quantities but the inverse dependence of the mobility on the diameter results in a negative derivative. It is convenient when carrying out the integration of Equation (15) to express the integral in terms of the dimensionless mobility x defined as:

$$x = \frac{2\pi\Lambda Z_p V}{q_s} \tag{16}$$

where $\Lambda = L/\ln(r_2/r_1)$ (17)

The transfer function Ω has an isosceles triangular shape as a function of x with the base of the triangle equal to 2ε.

$$
\begin{aligned}
\Omega(x) &= 0 & x < 1-\varepsilon \\
\Omega(x) &= 1 - \frac{1-x}{\varepsilon} & 1-\varepsilon \le x < 1 \\
\Omega(x) &= 1 + \frac{1-x}{\varepsilon} & 1 \le x < 1+\varepsilon \\
\Omega(x) &= 0 & x > 1+\varepsilon
\end{aligned}
\tag{18}
$$

The following expression for the right-hand size of Equation (15) is derived from Equations (9), (10) and (16).

$$\left|\frac{dD_p}{dZ_p}\right| \ dZ_p = \frac{dx}{x}\left|\frac{C_C'(D_p)}{C_C(D_p)} - \frac{1}{D_p}\right|. \tag{19}$$

Substituting from Equations 18 and 19 into Equation (15), one obtains the convolution integral in terms of the reduced mobility, x.

$$N_{cpc}(V) = \int_{1-\varepsilon}^1 \left(1 - \frac{(1-x)}{\varepsilon}\right)G(D_p(x))P(D_p(x))\frac{1}{x}\left|\frac{C_C'(D_p)}{C_C(D_p)} - \frac{1}{D_p}\right|^{-1} dx + \int_1^{1+\varepsilon}\left(1 + \frac{(1-x)}{\varepsilon}\right)G(D_p(x))P(D_p(x))\frac{1}{x}\left|\frac{C_C'(D_p)}{C_C(D_p)} - \frac{1}{D_p}\right|^{-1} dx \tag{20}$$

In general, the determination of the size distribution requires the inversion of Equation (20). For the case in which the size distribution is broad and changing slowly with diameter, an approximate expression can be obtained for $G(D_p)$. In this case, the transfer function varies much more rapidly with x than do the other functions appearing in the integrand of Equation (20). The other functions are, therefore, evaluated at the value of D_p corresponding to the peak in the transfer function, $x = 1$, for the given voltage. This leads to the following result:

$$N_{cpc}(V) = G(D_p(x=1))p(D_p(x=1))\left|\frac{C_C'(D_p(x=1))}{C_C(D_p(x=1))} - \frac{1}{D_p}\right|^{-1} \times \left[\int_{1-\varepsilon}^1\left(1 - \frac{(1-x)}{\varepsilon}\right)dx + \int_1^{1+\varepsilon}\left(1 + \frac{(1-x)}{\varepsilon}\right)dx\right] \tag{21}$$

The integral of the transfer function is ε, simply the area of a triangle with height 1 and base 2ε (see Equation (18)). Thus, from Equation (21), the following explicit expression approximates the size distribution:

$$G(D_p(x=1)) = \left[N_{cpc}(V)\left|\frac{C_C'(D_p(x=1))}{C_C(D_p(x=1))} - \frac{1}{D_p}\right|\right] / \left[\varepsilon \ P(D_p(x=1))\right] \tag{22}$$

The flow ratio number $\varepsilon = q_a/q_s$ sets the resolution of the measurement. The smaller the value of ε, which is often 0.1, the higher the measurement resolution. The single charging probability P increases with NP size up to a value of about 0.2 for 100 nm diameter NPs and is relatively constant with increasing size up to the maximum NP size of about 150 nm in this study. The term $B(D_p)$ in Equation (4) is roughly proportional to the inverse of the diameter and the exponent on the diameter ranges from 1 to 2 as one goes from the continuum limit to the free molecular limit.

Appendix 2

The ES-DMA-ICP-MS data can be corrected for overlapping charge states if a full size distribution is measured and a largest NP is detected (He & Dhaniyala, 2013). This largest size can be considered all singly charged NPs and the charge correction can work iteratively down to smaller sizes. The subscript format $D_{p,i,j,k}$ refers to the mobility diameter of a NP selected by the DMA with mobility i, charge j, and iteration k. For a smaller diameter, the data from the ICP-MS corresponds to singly and doubly charged NPs exiting the DMA.

$$M_{ICP-MS}(Z_{p,1}) = \varepsilon P(D_{p,1,1,1}) B^{-1}(D_{p,1,1,1}) H(D_{p,1,1,1}) + \varepsilon P(D_{p,1,2,1}) B^{-1}(D_{p,1,2,1}) H(D_{p,1,2,1}) \tag{23}$$

where $H(D_{p,i,j,k}) = \frac{dM(D_{p,i,j,k})}{dD_{p,i,j,k}}$. For the largest diameter, we assume that all of the ICP-MS response corresponds to singly charged NPs exiting the DMA.

$$M_{ICP-MS}(Z_{p,2}) = \varepsilon P(D_{p,2,1,1}) B^{-1}(D_{p,2,1,1}) H(D_{p,2,1,1}) \tag{24}$$

The two mobilities are selected such that $2Z_{p,2} = Z_{p,1}$ and therefore $D_{p,2,1,1} = D_{p,1,2,1}$, a doubly charged NP at the smaller mobility has the same diameter as a singly charged NP at the larger mobility, and $B(D_{p,1,2,1}) = B(D_{p,2,1,1})$, the derivative of mobility is greater for the doubly charged NP. Equation (24) can be solved for $H(D_{p,2,1,1})$ which can be substituted into Equation (23), because $H(D_{p,2,1,1}) = H(D_{p,1,2,1})$. The resulting solution is:

$$H(D_{p,1,1}) = \left[M_{cpc}(Z_{p,1}) - M_{cpc}(Z_{p,2}) P(D_{p,1,2,1}) / P(D_{p,2,1,1})\right] \left[B(D_{p,1,1,1}) / \varepsilon P(D_{p,1,1,1})\right] \tag{25}$$

An additional step is required after the first iteration if $D_{p,1,2,2}$ reaches a size that has been corrected as $D_{p,1,1,1}$ in a previous iteration. For example, if iteration one consists of $D_{p,1,1,1} = 150$ nm and $D_{p,1,2,1} = 240$ nm and iteration two consists of $D_{p,1,1,2} = 100$ nm and $D_{p,1,2,2} = 150$ nm, a correction will need to be made for $M_{ICP-MS}(Z_{p,2})$. Equation (23) remains nominally the same, though now it is iteration 2 (k = 2). Equation (24) is incorrect for iteration 2 because the ICP-MS response for the larger diameter consists of singly and doubly charged NPs.

$$M_{ICP-MS}(Z_{p,2,new}) = \varepsilon P(D_{p,2,1,2}) B^{-1}(D_{p,2,1,2}) H(D_{p,2,1,2}) + \varepsilon P(D_{p,1,2,1}) B^{-1}(D_{p,1,2,1}) H(D_{p,1,2,1}) \tag{26}$$

where $\varepsilon P(D_{p,1,2,1}) B^{-1}(D_{p,1,2,1}) H(D_{p,1,2,1})$ has been indirectly solved in a previous iteration.

$$M_{ICP-MS}(Z_{p,2,fix}) = M_{ICP-MS}(Z_{p,2,new}) - \varepsilon P(D_{p,1,2,1}) B^{-1}(D_{p,1,2,1}) H(D_{p,1,2,1}) \tag{27}$$

which can be solved using Equation (23).

$$M_{cpc}(Z_{p,2,new}) - \varepsilon P(D_{p,1,2,1}) B^{-1}(D_{p,1,2,1}) H(D_{p,1,2,1}) = \varepsilon P(D_{p,1,1,1}) B^{-1}(D_{p,1,1,1}) H(D_{p,1,1,1}) \tag{28}$$

This leaves an equation analogous to Equation (24):

$$M_{cpc}(Z_{p,2,fix}) = \varepsilon P(D_{p,2,1,2}) B^{-1}(D_{p,2,1,2}) H(D_{p,2,1,2}) \tag{29}$$

and Equation (23) (iteration 2) and 29 can be used to solve for $H(D_{p,1,1,2})$:

$$H(D_{p,1,1,2}) = \left[M_{cpc}(Z_{p,1}) - M_{cpc}(Z_{p,2,fix}) P(D_{p,1,2,2}) / P(D_{p,2,1,2})\right] \left[B(D_{p,1,1,2}) / \varepsilon P(D_{p,1,1,2})\right] \tag{30}$$

References

Ashfaq, M., Verma, N., & Khan, S. (2016). Copper/zinc bimetal nanoparticles-dispersed carbon nanofibers: A novel potential antibiotic material. *Materials Science & Engineering C- Materials for Biological Applications, 59*, 938–947. https://doi.org/10.1016/j.msec.2015.10.079

Bustos, A. R. M., & Winchester, M. R. (2016). Single-particle-ICP-MS advances. *Analytical and Bioanalytical Chemistry, 408*(19), 5051–5052. https://doi.org/10.1007/s00216-016-9638-1

Carazzone, C., Raml, R., & Pergantis, S. A. (2008). Nanoelectrospray ion mobility spectrometry online with inductively coupled plasma-mass spectrometry for sizing large proteins, DNA, and nanoparticles. *Analytical Chemistry, 80*(15), 5812–5818. https://doi.org/10.1021/ac7025578

Cargnello, M., Chen, C., Diroll, B. T., Doan-Nguyen, V. V. T., Gorte, R. J., & Murray, C. B. (2015). Efficient removal of organic ligands from supported nanocrystals by fast thermal annealing enables catalytic studies on well-defined active phases. *Journal of the American Chemical Society, 137*(21), 6906–6911. https://doi.org/10.1021/jacs.5b03333

Chan, S. C., & Barteau, M. A. (2005). Preparation of highly uniform Ag/TiO2 and Au/TiO2 supported nanoparticle catalysts by photodeposition. *Langmuir, 21*(12), 5588–5595. https://doi.org/10.1021/la046887k

Duelge, K. J., Parot, J., Hackley, V. A., & Zachariah, M. R. (2020). Quantifying protein aggregation kinetics using electrospray differential mobility analysis. *Journal of Pharmaceutical and Biomedical Analysis, 177*. https://doi.org/10.1016/j.jpba.2019.112845

Elzey, S., Tsai, D. H., Yu, L. L., Winchester, M. R., Kelley, M. E., & Hackley, V. A. (2013). Real-time size discrimination and elemental analysis of gold nanoparticles using ES-DMA coupled to ICP-ms. *Analytical and Bioanalytical Chemistry, 405*(7), 2279–2288. https://doi.org/10.1007/s00216-012-6617-z

Enache, D. I., Edwards, J. K., Landon, P., Solsona-Espriu, B., Carley, A. F., Herzing, A. A., Watanabe, M., Kiely, C. J., Knight, D. W., & Hutchings, G. J. (2006). Solvent-Free oxidation of primary alcohols to aldehydes using Au-Pd/TiO2 catalysts. *Science, 311*(5759), 362–365. https://doi.org/10.1126/science.1120560

Gommes, C. J., Prieto, G., Zecevic, J., Vanhalle, M., Goderis, B., de Jong, K. P., & de Jongh, P. E. (2015). Mesoscale characterization of nanoparticles distribution using X-ray scattering. *Angewandte Chemie International Edition, 54*(40), 11804–11808. https://doi.org/10.1002/anie.201505359

Gopalakrishnan, R., Meredith, M. J., Larriba-Andaluz, C., & Hogan, C. J. (2013). Brownian dynamics determination of the bipolar steady state charge distribution on spheres and non-spheres in the transition regime. *Journal of Aerosol Science, 63*, 126–145. https://doi.org/10.1016/j.jaerosci.2013.04.007

He, M. L., & Dhaniyala, S. (2013). A multiple charging correction algorithm for scanning electrical mobility spectrometer data. *Journal of Aerosol Science, 61*, 13–26. https://doi.org/10.1016/j.jaerosci.2013.03.007

Hess, A., Tarik, M., Losert, S., Ilari, G., & Ludwig, C. (2016). Measuring air borne nanoparticles for characterizing hyphenated RDD-SMPS-ICPMS instrumentation. *Journal of Aerosol Science, 92*, 130–141. https://doi.org/10.1016/j.jaerosci.2015.10.007

Holm, A., Goodman, E. D., Stenlid, J. H., Aitbekova, A., Zelaya, R., Diroll, B. T., Johnston-Peck, A. C., Kao, K. C., Frank, C. W., Pettersson, L. G. M., & Cargnello, M. (2020). Nanoscale spatial distribution of supported nanoparticles controls activity and stability in powder catalysts for CO oxidation and photocatalytic H-2 evolution. *Journal of the American Chemical Society, 142*(34), 14481–14494. https://doi.org/10.1021/jacs.0c03842

ISO. (2020). *Determination of particle size distribution - differential electrical mobility analysis for aerosol particles (ISO 15900). In. Geneva.*

Kim, J. H., Mulholland, G. W., Kukuck, S. R., & Pui, D. Y. H. (2005). Slip correction measurements of certified PSL nanoparticles using a nanometer differential mobility analyzer (nano-DMA) for knudsen number from 0.5 to 83. *Journal of Research of the National Institute of Standards and Technology, 110*(1), 31–54. https://doi.org/10.6028/jres.110.005

Knutson, E. O., & Whitby, K. T. (1975). Accurate measurement of aerosol electrical mobility moments. *Journal of Aerosol Science, 6*, 453–460. https://doi.org/10.1016/0021-8502(75)90061-0

Lee, J. P., Chen, D. C., Li, X. X., Yoo, S., Bottomley, L. A., El-Sayed, M. A., Park, S., & Liu, M. L. (2013). Well-organized raspberry-like Ag@Cu bimetal nanoparticles for highly reliable and reproducible surface-enhanced Raman scattering. *Nanoscale, 5*(23), 11620–11624. https://doi.org/10.1039/c3nr03363e

Liao, H. B., Fisher, A., & Xu, Z. C. J. (2015). Surface segregation in bimetallic nanoparticles: A critical issue in electrocatalyst engineering. *Small, 11*(27), 3221–3246. https://doi.org/10.1002/smll.201403380

Mulholland, G. W., Donnelly, M. K., Hagwood, C. R., Kukuck, S. R., Hackley, V. A., & Pui, D. Y. H. (2006). Measurement of 100 nm and 60 nm particle standards by differential mobility analysis. *Journal of Research of the National Institute of Standards and Technology, 111*(4), 257–312. https://doi.org/10.6028/jres.111.022

Munnik, P., Velthoen, M. E. Z., de Jongh, P. E., de Jong, K. P., & Gommes, C. J. (2014). Nanoparticle growth in supported nickel catalysts during methanation reaction-larger is better. *Angewandte Chemie International Edition, 53*(36), 9493–9497. https://doi.org/10.1002/anie.201404103

Myojo, T., Takaya, M., & Ono-Ogasawara, M. (2002). DMA as a gas converter from aerosol to "argonsol" for real-time chemical analysis using ICP-ms. *Aerosol Science and Technology, 36*(1), 76–83. https://doi.org/10.1080/027868202753339096

Pace, H. E., Rogers, N. J., Jarolimek, C., Coleman, V. A., Higgins, C. P., & Ranville, J. F. (2011). Determining transport efficiency for the purpose of counting and sizing nanoparticles via single particle inductively coupled plasma mass spectrometry. *Analytical Chemistry, 83*(24), 9361–9369. https://doi.org/10.1021/ac201952t

Peng, S., Lee, Y. M., Wang, C., Yin, H. F., Dai, S., & Sun, S. H. (2008). A Facile synthesis of monodisperse Au nanoparticles and their catalysis of CO oxidation. *Nano Research, 1*(3), 229–234. https://doi.org/10.1007/s12274-008-8026-3

Prieto, G., Meeldijk, J. D., de Jong, K. P., & de Jongh, P. E. (2013). Interplay between pore size and nanoparticle spatial distribution: Consequences for the stability of CuZn/SiO2 methanol synthesis catalysts. *Journal of Catalysis, 303*, 31–40. https://doi.org/10.1016/j.jcat.2013.02.023

Saetveit, N. J., Bajic, S. J., Baldwin, D. P., & Houk, R. S. (2008). Influence of particle size on fractionation with nanosecond and femtosecond laser ablation in brass by online differential mobility analysis and inductively coupled plasma mass spectrometry. *Journal of Analytical Atomic Spectrometry, 23*(1), 54–61. https://doi.org/10.1039/b709995a

Sankar, M., Dimitratos, N., Miedziak, P. J., Wells, P. P., Kiely, C. J., & Hutchings, G. J. (2012). Designing bimetallic catalysts for a green and sustainable future. *Chemical Society Reviews, 41*(24), 8099–8139. https://doi.org/10.1039/c2cs35296f

Sharma, G., Kumar, A., Sharma, S., Naushad, M., Dwivedi, R. P., Alothman, Z. A., & Mola, G. T. (2019). Novel development of nanoparticles to bimetallic nanoparticles and their composites: A review. *Journal of King Saud University Science, 31*(2), 257–269. https://doi.org/10.1016/j.jksus.2017.06.012

Tan, J. J., Cho, T. J., Tsai, D. H., Liu, J. Y., Pettibone, J. M., You, R. A., Hackley, V. A., & Zachariah, M. R. (2018). Surface modification of cisplatin-complexed gold nanoparticles and its influence on colloidal stability, drug loading, and drug release. *Langmuir, 34*(1), 154–163. https://doi.org/10.1021/acs.langmuir.7b02354

Tan, J. J., Liu, J. Y., Li, M. D., El Hadri, H., Hackley, V. A., & Zechariah, M. R. (2016). Electrospray-differential mobility hyphenated with single particle inductively coupled plasma mass spectrometry for characterization of nanoparticles and their aggregates. *Analytical Chemistry, 88*(17), 8548–8555. https://doi.org/10.1021/acs.analchem.6b01544

Tan, J. J., Yang, Y., El Hadri, H., Li, M. D., Hackley, V. A., & Zachariah, M. R. (2019). Fast quantification of nanorod geometry by DMA-spICP-MS. *Analyst, 144*(7), 2275–2283. https://doi.org/10.1039/c8an02250j

Taurozzi, J. S., Hackley, V. A., & Wiesner, M. R. (2013). A standardised approach for the dispersion of titanium dioxide nanoparticles in biological media. *Nanotoxicology, 7*(4), 389–401. https://doi.org/10.3109/17435390.2012.665506

Turner, M., Golovko, V. B., Vaughan, O. P. H., Abdulkin, P., Berenguer-Murcia, A., Tikhov, M. S., Johnson, B. F. G., & Lambert, R. M. (2008). Selective oxidation with dioxygen by gold nanoparticle catalysts derived from 55-atom clusters. *Nature, 454*(7207), 981–984. https://doi.org/10.1038/nature07194

Weyland, M., Midgley, P. A., & Thomas, J. M. (2001). Electron tomography of nanoparticle catalysts on porous supports: A new technique based on rutherford scattering. *The Journal of Physical Chemistry B, 105*(33), 7882–7886. https://doi.org/10.1021/jp011566s

White, R. J., Luque, R., Budarin, V. L., Clark, J. H., & Macquarrie, D. J. (2009). Supported metal nanoparticles on porous materials. Methods and applications. *Chemical Society Reviews, 38*(2), 481–494. https://doi.org/10.1039/b802654h

Wiedensohler, A. (1988). An approximation of the bipolar charge distribution for particles in the submicron size range. *Journal of Aerosol Science, 19*, 387–389. https://doi.org/10.1016/0021-8502(88)90278-9

Yang, Q., Liu, W. X., Wang, B. Q., Zhang, W. N., Zeng, X. Q., Zhang, C., Qin, Y. J., Sun, X. M., Wu, T. P., Liu, J. F., Huo, F. W., & Lu, J. (2017). Regulating the spatial distribution of metal nanoparticles within metal-organic frameworks to enhance catalytic efficiency. *Nature Communications, 8*. https://doi.org/10.1038/ncomms14429. Article 14429.